communications physics

Article

https://doi.org/10.1038/s42005-024-01597-7

High valley-degeneracy electron gas at double perovskite - strontium titanate interface

Zhao-Cai Wang[1,14], Lei Chen[2,14], Weiyao Zhao[3,4] ✉, Shuang-Shuang Li[1], Ying Zhang[1], Jing-Shi Ying[1], Shu-Juan Zhang[5], Fu-Sheng Luo[6], Ting-Wei Chen[1], Mao Ye[2], Lang Chen[7], Dan-Feng Li[8], David Cortie[9], Julie Karel[3,4], Kirrily Rule[9], Xiaolin Wang[10], Ji-Yan Dai[11] & Ren-Kui Zheng[2,12,13] ✉

Emergent phenomena such as two-dimensional electron gas (2DEG) and interfacial superconductivity and ferromagnetism are generally built on the interface between insulating oxide thin films and substrates, e.g., $LaAlO_3/SrTiO_3$, where the 2D profiles of these electronic states are precisely confined at the interface of two insulators. Herein we report a high-mobility electron gas state with unusual symmetry at the interface of the $Sr_2CrMoO_6/SrTiO_3$ (110) heterostructures, the fermiology of which follows the cubic crystallographic symmetry rather than the two-dimensional interface itself, resulting in the identical Shubnikov-de Haas oscillations with applied magnetic field along all the twelve equivalent [110] crystallographic directions of $SrTiO_3$, distinctly different from the 2D nature of the electron gas reported previously. Neutron diffraction verifies the predicted ferrimagnetic ordering between Cr and Mo moments. This, together with the magnetic hysteresis loops and negative magnetoresistance in low-field region, suggests possible spin polarization of itinerant electrons. Therefore, a quasi-3D profile, high mobility (up to $10^4\ cm^2\ V^{-1}\ s^{-1}$) and possibly spin polarized electronic state is observed in the double-perovskite-based oxide heterostructures. This finding of the electronic properties in $Sr_2CrMoO_6/SrTiO_3$ (110) heterostructure expands the knowledge of interfacial physics, as well as shines light on oxide-based electronics and spintronics research.

The two-dimensional electron gas (2DEG) at the interface of oxide heterostructures has drawn increasing attention recently[1–9]; 2D-confined electrons dominate the physical properties and introduce a range of interesting phenomena including spin polarization[7,8], superconductivity[6,9], and Wigner crystal states[10]. There are several important symmetry parameters to the physical properties of the heterostructures, e.g., inversion symmetry, time reversal symmetry, and Gauge symmetry, breaking of which corresponds to the charge transfer, spin polarization, and superconducting state at the interface. Moreover, the tunability of the carrier density at the interface offers an interest platform for Rashba physics, in which the strength of the spin-orbit coupling and asymmetric potential on different sides can be manipulated by a gate voltage[11,12].

Sr_2CrMoO_6 (SCMO) is a double perovskite crystallized in the cubic structure with the $F_{m\bar{3}m}$ space group, usually known as a half metal with a fully spin-polarized Fermi surface[13,14], due to the ferrimagnetic ordering between the Cr^{3+} and Mo^{5+} ions ($T_C \sim 450$ K)[15,16]. Previous studies of its isostructural double perovskites, e.g., Sr_2CrWO_6 and Sr_2FeMoO_6, where one important feature is the ordered distribution of the B-sites cations (Cr/W, or Fe/Mo), mainly focused on the large room-temperature negative magnetoresistance (MR)[17,18]. MR is defined as $\left[\rho(B) - \rho(0)\right]/\rho(0)$, where $\rho(B)$ and $\rho(0)$ are the resistivity (ρ) in an external magnetic field B and $B = 0$ T, respectively. Regardless of the predicted half-metallic ground states in theoretical prediction, semiconducting behavior is always found in solid-state-reaction synthesized double perovskites like Sr_2CrWO_6 and SCMO, possibly due to the high Cr-Mo/W antisite defect levels[19]. Nevertheless, epitaxial thin films of Sr_2CrWO_6[20] and SCMO[14] on $SrTiO_3$ (STO) (001) substrates tell alternative stories with metallic conductivity down to 1.8 K, ultrahigh mobility, and a large positive MR at low temperatures. These high-mobility conducting electronic state share the similarities with STO-based 2DEG.

Here, we investigated the Shubnikov-de Haas (SdH) oscillations of the epitaxial SCMO/STO (110) heterostructures to reveal the Fermi surface profile in this system. Angular dependent SdH analyses reveal that the Fermi pockets contributing to SdH oscillations exist at every

A full list of affiliations appears at the end of the paper. ✉e-mail: weiyao.zhao@monash.edu; zrk@ustc.edu

equivalent [110] direction, following the cubic crystallographic symmetry. A quasi-three-dimensional (quasi-3D) morphology profile is present in *k* space. Moreover, negative MR and magnetic hysteresis loops were observed in low-field region, the combination of which may suggest a spin-polarized electron gas state in the SCMO/STO (110) heterostructure. This unexpected electron gas state could build a playground for designing and controlling the properties of transition metal oxide heterostructures.

Results and discussion

Structure

High-quality SCMO epitaxial thin films were grown on STO (110) substrates via the pulsed laser deposition method. The STO (110) substrates and SCMO epitaxial films possess in-plane crystallographic anisotropy, which means that the two in-plane perpendicular edges are parallel to the [1$\bar{1}$0] and [001] directions, respectively, as schematically illustrated in Fig. 1a. The atomic force microscopy (AFM) image in Fig. 1a shows the atomically flat surface of an as-grown SCMO film, with a root mean square roughness of ~ 80 pm. The X-ray diffraction (XRD) θ-2θ scan pattern of the SCMO film is shown in Fig. 1c, in which the SCMO (220) and (440) diffraction peaks are observed on the left shoulder of the sharp STO (110) and (220) diffraction peaks. A zoomed-in pattern near the SCMO (220) peak is shown in the inset of Fig. 1c, in which the Keissig fringes are signature of smooth surface of the film. The thin-film thickness calculated from the fringes is ~35 nm. The XRD rocking curve taken on the SCMO (220) diffraction peak yields a narrow full width at half maximum (FWHM) of 0.09° (Supplementary Note 1 for complementary data analysis of Fig. 1a), implying excellent crystalline quality of the film. Further, the X-ray reciprocal space mapping pattern (Fig. 1d), φ-scan patterns (Supplementary Note 1 for complementary data analysis of Fig. 1b), and high-resolution high-angle annular dark-field (HAADF) scanning transmission electron microscopy (STEM) images (Supplementary Note 1 for complementary data analysis of Fig. 2) reveal the coherent epitaxial growth of the SCMO film on the STO substrate and high quality of the interface.

Magnetotransport

Our previous report evidenced that high-quality SCMO/STO (001) heterostructures show metallic resistance behaviors and ultrahigh mobility at low temperatures[14]. However, as shown in Supplementary Note 2 for complementary data analysis of Fig. 3, the high-quality SCMO thin films grown on $(LaAlO_3)_{0.3}(Sr_2AlTaO_6)_{0.7}$ (LSAT) (110), LAO (110), and MgO (110) substrates using the same thin-film growth condition show semiconducting resistivity behaviors and negative MR, which are similar to those observed in polycrystalline SCMO samples[19]. Note that a bare STO substrate experienced the same high temperature and high vacuum deposition process showing semiconducting resistance behaviors due to oxygen vacancies in the STO substrate, as shown in Supplementary Note 2 for complementary data analysis of Fig. 4. Although both SCMO film and oxygen-deficient STO substrate show semiconducting resistance behaviors, the SCMO/STO (110) heterostructure shows good metallic resistivity behavior, as shown in Supplementary Note 2 for complementary data analysis of Fig. 5a. We further performed two-terminal resistance measurements of the thin-film sample along the thickness direction of the SCMO/STO (110) heterostructure where the bottom electrode is made at the backside of the STO substrate. The results are shown in Supplementary Note 3 for complementary data analysis of Fig. 6. The resistance also shows semiconducting characteristics with decreasing temperature and exceeds the measurement limit of our PPMS (10 MΩ) below 150 K. Therefore, it is reasonable to speculate that the interface between SCMO and STO has accumulated electrons to form a highly conducting interfacial layer, as schematically shown in Fig. 1b. These metallic resistivity behaviors are analogous to the 2DEG in LAO/STO heterostructures[1], implying that they may share similar mechanisms.

As shown in Fig. 1e, f, the sheet resistance $R_{\square}$ vs. B curves up to 14 T are measured from 1.8 to 5 K, employing a Hall-bar configuration on the top surface of the 35-nm SCMO/STO (110) heterostructure, as sketched in the insets of Fig. 1e, f. Here, the sheet resistance is used instead of resistivity, due to the relatively complicated conducting channels. Traditionally, the magnetotransport measurements on 2DEG systems are conducted with the direction of B perpendicular to the electron gas plane[21]. Figure 1e shows $R_{\square}$ vs. B curves with the magnetic field applied along the [110] direction, and

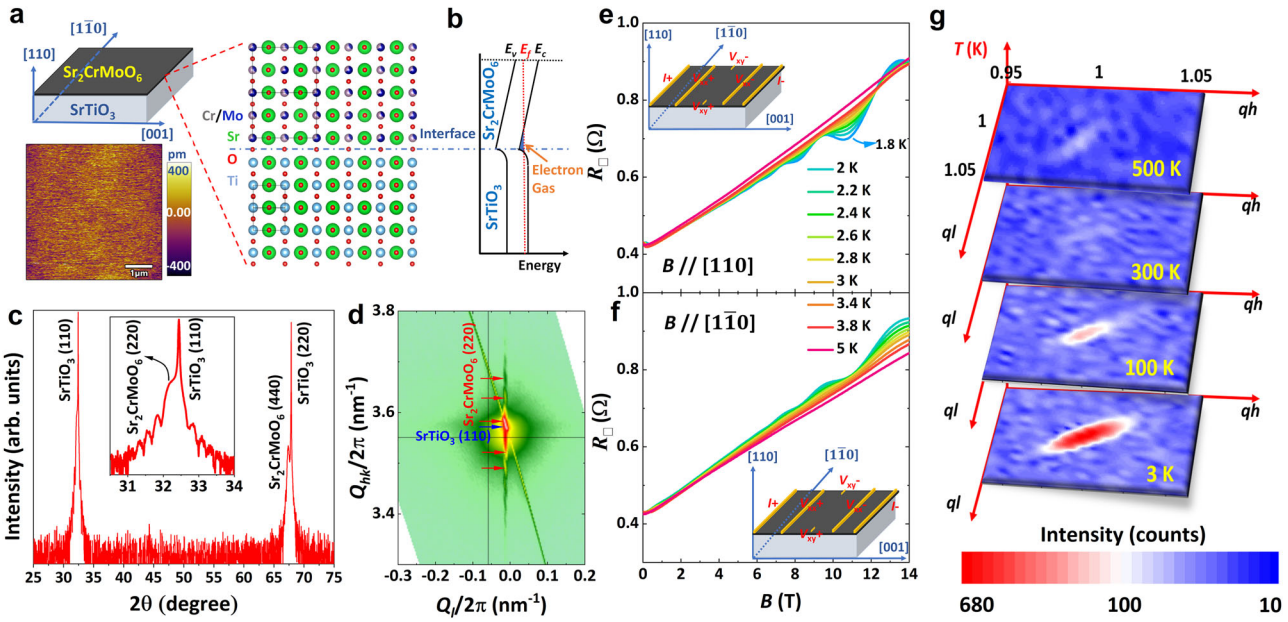

Fig. 1 | Characterization of Sr_2CrMoO_6 thin films. a The interfacial crystal structure sketch between Sr_2CrMoO_6 film and $SrTiO_3$ substrate and atomic force microscopy image. **b** The electronic structure sketch near $Sr_2CrMoO_6/SrTiO_3$ interface, which allows electron gas state. **c** Room temperature X-ray diffraction patterns for a 35-nm Sr_2CrMoO_6 film. Inset: zoom-in plot near the Sr_2CrMoO_6 (220) diffraction peak. **d** X-ray reciprocal space mapping of the Sr_2CrMoO_6 film. **e** Low-temperature sheet resistance $R_{\square}$ vs. magnetic field B curves, with the direction of the magnetic field along the [110] and [1$\bar{1}$0] directions, respectively. **f** Temperature-dependent neutron diffraction reciprocal space mapping of the magnetic peak.

perpendicular to the SCMO/STO interface, while the electric current is always applied along the [001] direction. Positive MR increases approximately linearly with external B, which is similar to the case of SCMO/STO (001) heterostructures. The mobility fluctuation model in ref. 14 can be therefore employed here to explain the linear MR, which consists of two important aspects: (1) the high mobility carriers in sufficiently large external B follows cyclotron orbit movement, which drifts in the electric field; 2) Cr-Mo antisite defects create a slow-varying potential, yielding the drifting orbits that wind around the low-mobility islands. The other important feature of the $R_{\square}$ vs. B curves in Fig. 1e is the resistance oscillation patterns superimposed on the roughly linear backgrounds, which are weakened upon heating, and negligible at ~3.8 K. The oscillations originate from the periodic modulation (Landau quantization) of allowed electronic states in external B field, denoted as SdH oscillations. As aforementioned, the electric current is applied along the [001] direction, which leaves two equivalent [110] and [1$\bar{1}$0] directions in the (001) plane of SCMO itself, however, in the SCMO/STO (110) heterostructure these two vectors are actually nonequivalent because of the broken inversion symmetry at the interface, e.g., the [110] direction is perpendicular to the interface/electron gas plane, while the [1$\bar{1}$0] direction lies in the interfacial plane. What is particularly interesting and unexpected is that the SdH oscillations are also observed with external B // [1$\bar{1}$0] direction, namely, B // electron gas plane, as shown in Fig. 1f. Such strong SdH oscillations with B // interface are rarely observed in oxide heterostructures including the well-known LAO/STO[1], EuO/$KTaO_3$[8], and γ-Al_2O_3/STO[22] heterostructures. Thus, we observed electron-gas-like behaviors in the SCMO/STO (110) heterostructure, which, however, is not a typical 2DEG system. The details of these oscillation patterns will be further discussed in later sections.

Neutron diffraction

The proposed Cr-Mo antisite defects not only have critical influences on electronic transport behaviors but also play a dominant role in the magnetic properties. For B-site cation ordered double perovskites with negligible disorder, the ferrimagnetic ordering between the two B-site cation moments usually occurs at high temperatures[15,16]. However, the strict ferrimagnetic ordering between the two B-site cation moments will be significantly affected by the antisite disorder, e.g., the saturation moment per formula is ~2.9 μ_B for B-site cation ordered Sr_2FeMoO_6 samples, and ~0.8 μ_B for disordered ones; additionally, the magnetic peak intensity of neutron diffraction (which is proportional to the overall magnetic order parameter) increases fast to a near-saturation value below T_C in well-ordered samples, however, increases slowly upon cooling for disordered ones[23]. For SCMO films on STO (001) substrates, the saturation moment is ~1.5 μ_B/f.u., smaller than 2 μ_B/f.u. of perfect Cr-Mo dimer[14]. The magnetic properties of the SCMO/STO (110) heterostructure are shown in Supplementary Note 4 for complementary data analysis of Fig. 7. Further, we employed the thermal triple-axis neutron spectrometer Taipan[24], which provides more detection sensitivity than that of regular neutron diffractometer, to study the magnetic structure of the SCMO (110) thin-film sample (Supplementary Note 5 for complementary data analysis of Fig. 8). As shown in Fig. 1g, a strong SCMO (111) magnetic peak was observed at the base temperature (3 K). This peak superimposes on the SCMO (111) structural diffraction peak, which is a structurally allowed nuclear reflection and whose intensity is much weaker than the magnetic signal (Supplementary Note 5 for complementary data analysis of Fig. 8). The (111) magnetic peak suggests ferromagnetic alignment of moments among Cr ions, and among Mo ions, which supports the calculated G-type ferrimagnetic spin configuration[14]. Note that, previous work has demonstrated that spin-polarized 2DEG can be obtained at the interface by introducing magnetically ordered oxides, e.g., insertion of 2 unit cells of $EuTiO_3$ magnetic layer between LAO and STO introduces spin polarization of 2DEG[25], EuO/$KTaO_3$ interface shows spin-polarized 2DEG below the ferromagnetic ordering temperature of EuO (~70 K)[8]. Upon the influences of the interfacial Cr^{3+}, Mo^{5+}, and Ti^{3+} spins, the SCMO/STO (110) heterostructure shows considerable low-field negative MR (~-50%) at low temperatures (Supplementary Note 6 for complementary data analysis of Fig. 9).

Shubnikov-de Haas oscillation

The background-subtracted SdH oscillation patterns are shown in Fig. 2a, b, in which the lowest temperature was extended to 100 mK. The oscillation patterns are plotted against 1/B, on which the oscillations show periodicity. With the direction of B perpendicular to the interface (i.e., along the [110] direction, B // [110]), the itinerant electrons form cyclotron orbits, which drift in the electric field direction, as sketched in the left hand of Fig. 2e. With the direction of B parallel to the interface (i.e., along the [1$\bar{1}$0] direction, B // [1$\bar{1}$0]), the cyclotron orbits are perpendicular to the interface, as sketched in the right hand of Fig. 2e, meaning that the thickness of the electron gas layer is large enough to accommodate electron cyclotron orbits. The itinerant electrons might be injected into the semiconducting SCMO film to some degree to complete the cyclotron motion. With large enough magnetic fields, the allowed states for electrons are modulated, resulting in the oscillation patterns that can be described by the Lifshitz-Kosevich (LK) formula:

$$\frac{\Delta\rho}{\rho(0)} = \frac{5}{2}\left(\frac{B}{2F}\right)^{\frac{1}{2}} R_T R_D R_S \cos\left[2\pi\left(\frac{F}{B} + \gamma - \delta\right)\right]$$

where $R_T = \alpha T m^*/B \sinh(\alpha T m^*/B)$, $R_D = \exp(-\alpha T_D m^*/B)$, and $R_S = \cos(\alpha g m^*/2)$. Here, m^* is the ratio of the effective cyclotron mass to the free electron mass m_e; g is the g-factor; T_D is the Dingle temperature; and $\alpha = (2\pi^2 k_B m_e)/\hbar e$, where k_B is Boltzmann constant, $\hbar$ is the reduced Planck constant, and e is the elementary charge. The oscillation of $\Delta\rho$ is described by the cosine term with a phase factor $\gamma - \delta$, in which $\delta = 0$ for 2D systems, and ±1/8 for 3D Fermi pockets, $\gamma = 1/2 - \Phi_B/2\pi$, where Φ_B is the Berry phase. For electron systems, the Berry phase is usually zero. According to the Onsager-Lifshitz equation, the frequency of quantum oscillations, $F = (\varphi_0/2\pi^2)A_S$, where A_S is the extremal cross-sectional area of the Fermi surface perpendicular to the magnetic field, and φ_0 is the magnetic flux quantum. The temperature and magnetic field damping factor R_T and R_D are related to the cyclotron mass and quantum relaxion time of the electron system. The corresponding fast Fourier transform (FFT) spectra of the oscillation patterns are shown in Fig. 2c, d, respectively, from which one may notice that the oscillation frequencies for both directions of B are ~33.4 T. Employing the Onsager-Lifshitz relation, the cross-sectional area of the two Fermi pockets are both $A_S \sim 3.2 \times 10^{-3}$ Å^{-2}. Thus, assuming ring shape of the pockets, the Fermi vector of $k_F \sim 3.2 \times 10^{-2}$ Å^{-1} could be obtained. Further, the FFT amplitudes are representative of the SdH oscillation amplitudes, which can be employed to fit the temperature damping factor R_T, as shown in Fig. 2f. The effective electron mass along the [110] and [1$\bar{1}$0] directions, obtained from the fittings, are 1.80 and 1.75 m_e, respectively. Thus, one can obtain the Fermi velocity $v_F = \hbar k_F/m^* \sim 2.0 \times 10^4$ m/s for both directions of B. Further, using the obtained electron mass, we fitted the magnetic field damping factor R_D at 0.1 K and 1 K, as shown in Fig. 2g. The obtained T_D are: 10 and 7.7 K for oscillations at 0.1 and 1 K along the (110) direction; 16.8 and 14.7 K for oscillations at 0.1 and 1 K along the [1$\bar{1}$0] direction. The quantum relaxation time and quantum mobility at 0.1 K can also be obtained by $\tau = \hbar/2\pi k_B T_D$ (1.2 and 0.77 ps for the [110] and [1$\bar{1}$0] directions) and $\mu_Q = e\tau/m^*$ (2100 and 1250 cm^2 V^{-1} s^{-1} for the [110] and [1$\bar{1}$0] directions), respectively. Note that, the Hall mobility μ_{Hall} (1×10^4 cm^2 V^{-1} s^{-1} at 1.8 K) is much larger than μ_Q, which suggests that the screened-Coulomb scattering is the dominant scattering source for electrons[26]. These Fermi pocket parameters obtained from the SdH oscillations for B // [110] and B // [1$\bar{1}$0] are roughly the same, which suggests that the SdH oscillation follows the crystallographic (C_4) symmetry, but not the conventional C_2 symmetry of the interface.

Angle dependent Shubnikov-de Haas oscillation

Angular θ-dependent SdH oscillation measurements are employed to further understand the electron state at the SCMO/STO interface. During the rotation of the thin-film sample around the (001) axis, the direction of B is parallel to the [110] direction (B // [110]) and remains unchanged during the rotation of the sample. The rotation starts from the [110] direction, denoted

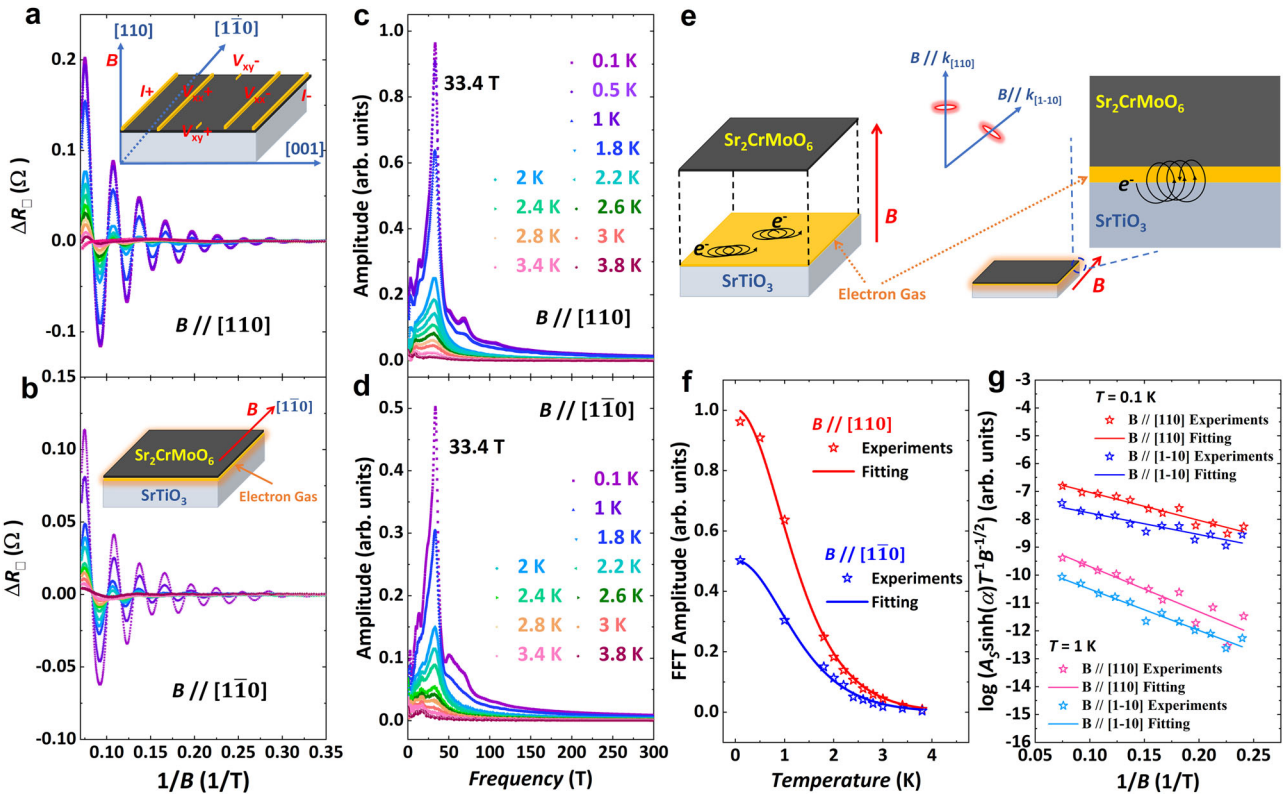

Fig. 2 | Shubnikov-de Haas oscillation analyses. a The background-subtracted Shubnikov-de Haas oscillation patterns, as measured by applying magnetic fields along the [110] direction. **b** The Shubnikov-de Haas oscillation patterns, as measured by applying magnetic fields along the [1$\bar{1}$0] direction. **c**, **d** The fast Fourier transform (FFT) spectra related to the oscillations in Panels (**a**, **b**), respectively. **e** A sketch of the electron cyclotron orbit at the interface. **f** The thermal damping factor fitting of the Shubnikov-de Haas oscillations. The error bars are smaller than the symbols. **g** The magnetic field damping factor fitting of the Shubnikov-de Haas oscillations. The error bars are smaller than the symbols.

as 0°; to the [1$\bar{1}$0] direction, denoted as 90°; then to the [$\bar{1}$1$\bar{0}$] and [$\bar{1}$10] directions, and finally back to the [110] direction; as sketched in Fig. 3a. The sheet resistance vs. B curves in the first quadrant ($0° \le \theta \le 90°$) are shown in Fig. 3b, in which the oscillation amplitude first decreases with the rotation angle from 0°, reaches the weakest amplitude at $\theta = 45°$, and increases with θ until 90°. As shown in Fig. 2a, b, the SdH oscillation amplitude at $\theta = 0°$ (B // [110]) and 90° (B // [1$\bar{1}$0]) are indeed rather strong, which means that one may observe the same oscillation patterns at $\theta = 180°$ and 270°, based on the C_4 symmetry of the (001) plane of both the SCMO film and STO substrate. Figure 3c shows the background-subtracted SdH oscillation patterns in the 0°—360° rotation region plotted against 1/B in the heat map format to emphasize the C_4 symmetry. The strongest oscillation amplitude (showing in red) occurs at $\theta = 0°$, 90°, 180°, and 270°, which are all along the equivalent [110] crystallographic directions. The FFT map (Fig. 3d) tells the same story.

It's worth mentioning that the STO with sufficient oxygen vacancies may also show SdH oscillations at a similar low-temperature range, e.g., 2 K. We heat-treated a STO (110) single-crystal substrate at 1000 °C under 1×10^{-9} Pa for 24 h using our molecular beam epitaxy (MBE) system (Dr. Eberl MBE-Komponenten GmbH, Germany). Such a high temperature and high vacuum condition is sufficient to remove a significant portion of oxygen atoms from the STO substrate to make it conduct. We conducted electronic transport measurements on a treated STO (110) substrate and show the results in Supplementary Note 7 for Fig. 10a, b, c. The sample shows metallic behavior upon cooling to 2 K (Supplementary Note7 for Figure 10a), which demonstrates that oxygen atoms have been sufficiently extracted from the pristine STO substrate. Angular-dependent MR vs. B curves for different rotation angles (θ) for the treated STO (110) substrate are shown in Supplementary Note 7 for Fig. 10b, where SdH oscillations are observed for $\theta \le 40°$ and the oscillation amplitude becomes weaker with increasing θ. Moreover, oscillations disappear for $\theta > 40°$ and MR becomes negative for $\theta = 90°$ (the direction of the magnetic field parallel to the [1-10] direction, as schematically shown in the inset of Supplementary Note 7 for Fig. 10b. A magnified view of the MR vs. B curves is shown in Supplementary Note 7 for Fig. 10c. These magneto-transport features are in sharp contrast to those of the SCMO/STO (110) heterostructure shown in Supplementary Note 7 for Fig. 10d, where the oscillation for $\theta = 90°$ is still rather strong and there is no negative MR. Therefore, the observed peculiar angular-dependent SdH oscillations are related to the interface rather than oxygen-deficient STO substrates.

To further verify this point, we performed rotation angle φ-dependent SdH measurements, starting from the [001] direction, denoted as 0°; to the [110] direction, denoted as 90°; then to the [00$\bar{1}$] and [1$\bar{1}$0] directions; and finally, back to the [001] direction, as sketched in Fig. 4a. Again, before the rotation of the thin-film sample around the (1$\bar{1}$0) axis, the direction of B is parallel to the [001] direction (B // [001]) and remains unchanged during the rotation of sample. Note that, the electric current is still along the [001] direction. The background-subtracted oscillations in the form of heat map are shown in Fig. 4b, in which the most obvious oscillations are still along the [110] and [1$\bar{1}$0] directions. In fact, during the rotation process, only 2 equivalent (110) vectors, namely (110) and (1$\bar{1}$0), are on the rotation route, which results in a two-fold symmetry in Fig. 4b. Also, the FFT map for the φ rotation verifies the two-fold symmetry, as shown in Fig. 4e. Another point is that the oscillation amplitude seems to be damping slower with φ than with θ, e.g., the oscillation vanishes completely at $\theta = 45°$ (Fig. 3c), but still possesses enough intensity at $\varphi = 45°$, as indicated by the black dash line in Fig. 4b. Based on Fig. 3c, one may find that the noticeable SdH oscillations below 14 T are observed within an angle (between the direction of B and the normal vector of the Fermi pocket) range, which is approximately 35°. Keeping this in mind, there are 12 equivalent pockets (valley degeneracy $v_v = 12$) in the Brillouin zone, some of which, e.g., the pocket on $k_{(011)}$ as

sketched in Fig. 4c, might contribute to the oscillations on the φ rotation route. Therefore, we calculated the angle Θ between the direction of B and any equivalent [110] directions during the φ rotation, which is summarized in Fig. 4d. The oscillation frequencies F follows the cosine rule in 2D pocket scenario: $F(\Theta) = F(0°)/\cos\Theta$, which is an even function of Θ. Here, Θ is the effective angle between the direction of the magnetic field and the contributed pockets. Therefore, the two light-pink area in Fig. 4d indicate the possible contributing pockets on φ rotation route. To check this point, we plot the FFT curves in Fig. 4f, using the data shown in a chosen area of the FFT spectrum map (the yellow box in Fig. 4e). Note that, constants are multiplied for the low-angle spectra, to enhance the visibility in Fig. 4f. The main peak positions in Fig. 4f are summarized in Fig. 4g, as blue stars, which agrees with the red and black $F(\Theta)$ simulation curves quite well. Specifically, in high φ region ($60° \le \varphi \le 90°$), the pockets on $k_{(110)}$ and $k_{(-1-10)}$ contribute mainly to the SdH oscillations; which turns to the degenerate $k_{(0-1-1)}$, $k_{(-10-1)}$, $k_{(101)}$, and $k_{(011)}$ dominance in low φ region ($20° \le \varphi < 60°$) (Fig. 4g). Moreover, some low-frequency oscillations are also detected in the FFT spectra (Fig. 4f), whose amplitudes are much weaker than those of the main oscillation peaks. For instance, the background-subtracted oscillation patterns at $\varphi = 45°$ and $T = 1.8$ K is plotted against B (black dots), and carefully fitted using the three-frequency linear-superposition LK formula (red curve) in Fig. 4h. The fitting frequencies agree with the FFT results in Fig. 4f, in which the low frequencies could be attributed to the tunneling effect between the spin polarized pockets in form of "figure of 8"[27]. As illustrated in Fig. 4i, the contributing pockets possess different angles with respect to the direction of B (i.e., $k_{[001]}$), which would result in different "effective pockets" perpendicular to B, following the cosine rule. The tunneling effect between the two pockets, or among multiple pockets could contribute to the low frequencies in the FFT spectra (Fig. 4f). Further, SdH oscillation measurements were also conducted by rotating the thin-film sample around the (110) axis, with B // [001] (i.e., ψ-dependent SdH oscillations). The oscillations manifest similar results as the above discussion, as shown in Supplementary Note 8 for complementary data analysis of Fig. 11.

Symmetry analysis of Fermi surface

The finding of θ-, φ-, and ψ-dependent SdH oscillations within an angle range (~35°) along the twelve equivalent [110] crystallographic directions demonstrates that the interfacial electronic states contributing to the SdH oscillations are 2D-like Fermi pockets, as schematically illustrated by the shadowed red circles in Fig. 3e. Moreover, the oscillations occur only when the direction of the magnetic field is parallel to the twelve equivalent [110] crystallographic directions. Therefore, there are twelve 2D-like Fermi pockets whose normal vectors are approximately parallel to the twelve equivalent [110] crystallographic directions. These peculiar Fermi surface (Fig. 3e) indicates that the electron gas state at the interface is not 2D/quasi-2D or strictly 3D. Here, we use quasi-3D to describe the electron gas states. Such a band renormalization in the SCMO/STO heterostructure tells the difference against the electronic states of oxygen-deficient STO single crystals whose conduction edge contributes to an ellipsoid-shape Fermi surface around Γ point, which should lead to continuously changing oscillation frequency follow quadratic function.

The equivalent [110] direction-preferred SdH oscillations demonstrate an unusual electronic state consisting of twelve 2D-like Fermi pockets in the SCMO/STO heterostructures, which is an interfacial effect, and different from either STO or SCMO band structures, e.g., the conduction band edge of STO contains multiple 3D pockets[28,29], the SCMO exhibits two large spin-polarized electrons pockets[13,14], surrounding its Γ point in the Brillouin zone. To demonstrate the full picture, we further discuss more electronic transport features of this system. (1) The R-T curve and Hall angle show T^2 dependence (Supplementary Note 2 for complementary data analysis of Fig. 5b), which indicates the Fermi liquid behaviors, where the electron-electron scattering is more important than the electron-phonon scattering. (2) The

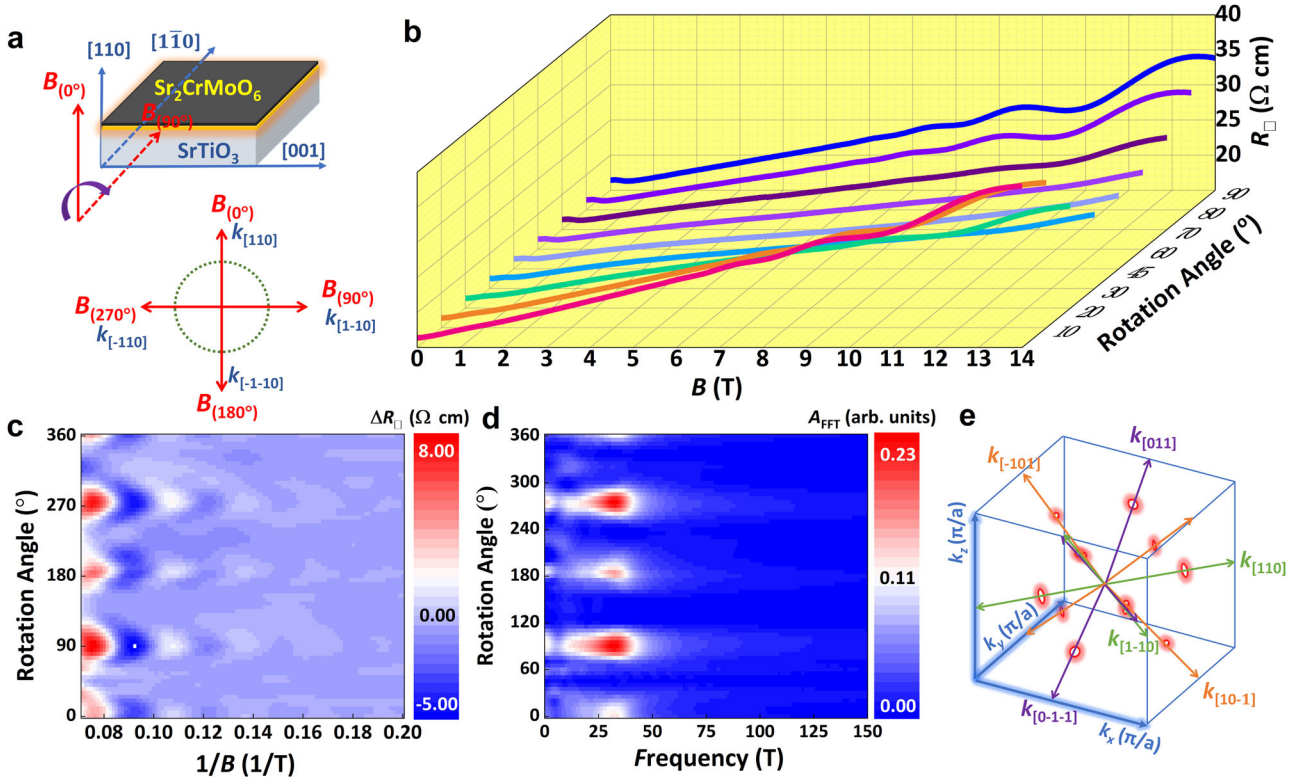

Fig. 3 | Rotation angle measurements of Shubnikov-de Haas oscillations in the (001) plane. a The sketch of the rotation plane. **b** The sheet resistance $R_{\square}$ vs. magnetic field B curves in the rotation angel $\theta = 0°$-$90°$ region. **c** The background-subtracted oscillation patterns are plotted in the heat map format. **d** The fast Fourier transform (FFT) spectra map of the oscillation patterns in Panel (**c**). **e** A sketch of the possible electronic states for the electron gas system at the $Sr_2CrMoO_6/SrTiO_3$ interface. The three shadowed blue lines represent the coordinates in moment space. The twelve shadowed red circles represent the 2D-like Fermi pocket.

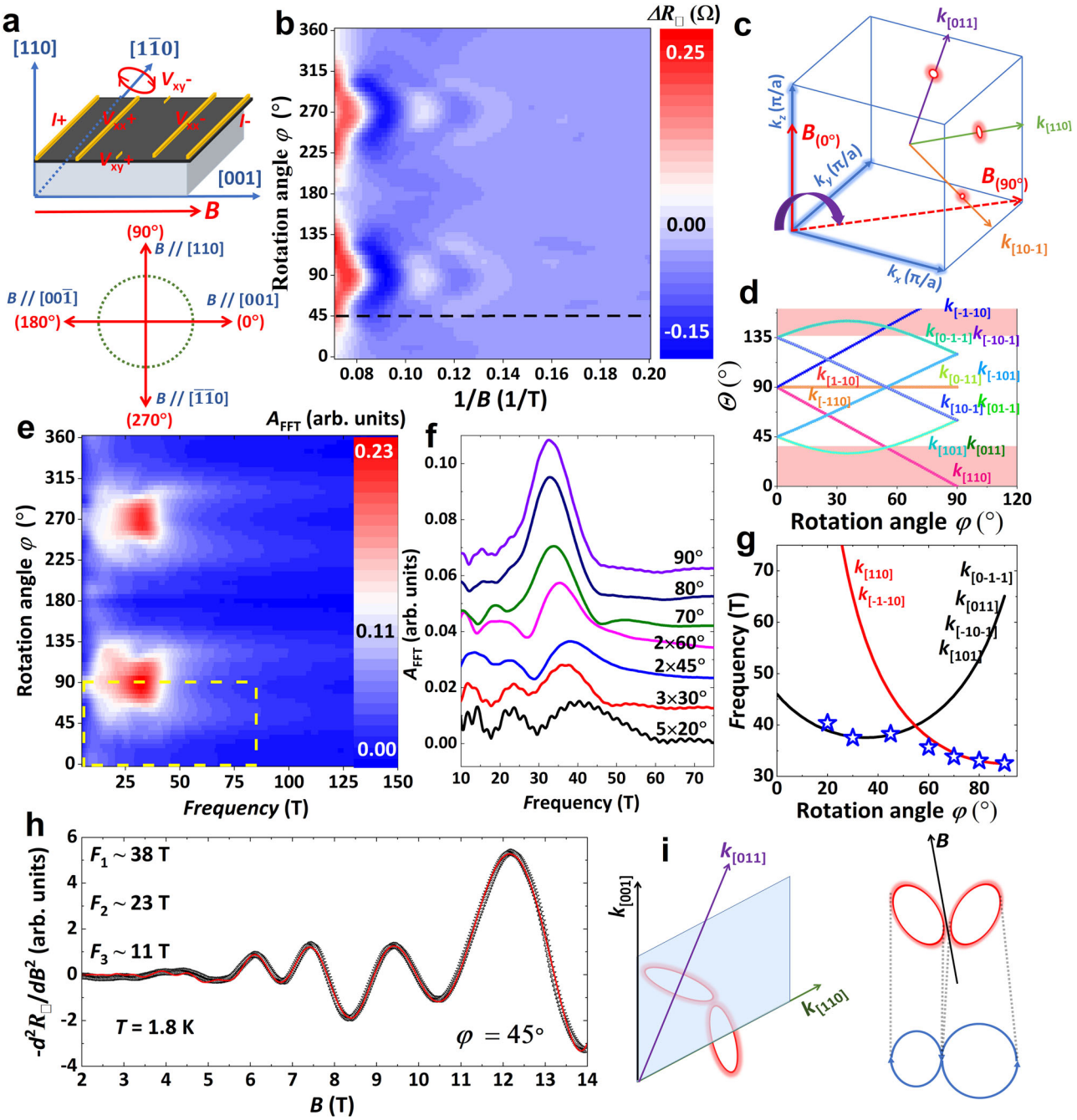

Fig. 4 | Rotation angle measurements of φ-Shubnikov-de Haas oscillations in the (1$\bar{1}$0) plane. a The sketch of the rotation plane. **b** Shubnikov-de Haas oscillation pattern in heat map format. **c** A sketch of the rotation plane and the contributed electron Fermi pockets. **d** The effective angle between the direction of the magnetic field and the contributed pockets, is plotted against the rotation angle φ in the (1 $\bar{1}$0) plane. **e** The fast Fourier transform (FFT) spectra map linked to Panel (**b**). **f** The fast Fourier transform (FFT) spectra of the yellow-box area in Panel (**e**), in which some of the weak patterns are multiplied by constants. The main frequencies in Panel (**f**) are summarized in Panel (**g**), which can be fitted with the 2D-pocket cosine rule. **h** Lifshitz-Kosevich (LK) formula fitting of the oscillation at $\varphi = 45°$. **I** A sketch for the possible electron pocket tunneling.

Hall effect contributes to the linear ρ_{xy} vs. B curves between ± 14 T fields, from which one may obtain the carrier's density $n_{Hall} \sim 1.15 \times 10^{17}$ cm^{-2} and mobility $\mu_{Hall} \sim 1 \times 10^4$ cm^2 V^{-1} s^{-1} at 1.8 K (Supplementary Note 2 for complementary data analysis of Fig. 5c). From the SdH oscillations, one may calculate $n_{2D} = Fv_v v_s e/h \sim 9.7 \times 10^{13}$ cm^{-2}, where F, v_v, v_s, e, and h are oscillation frequency, valley and spin degeneracy ($v_v = 12$, and $v_s = 1$), electron charge and Planck's constant, respectively. Therefore, the carriers in the STO and SCMO also contribute to the Hall effect. (3) With the coexistence of interfacial states and STO states, the overall conductivity in the SCMO/STO heterostructure is excellent, e.g., 0.45 Ω at 1.8 K and 7 Ω at 300 K, which could provide a low-dissipation spin-polarized electron source for potential applications, such as spin transfer torque devices.

Conclusions

Combined, we fabricated a high-quality 35-nm SCMO/STO (110) heterostructure with high mobility electron gas (1×10^4 cm^2 V^{-1} s^{-1}) at the interface. Surprisingly, at low temperatures, the SdH oscillations occur at all twelve equivalent [110] crystallographic directions including the in-plane (1$\bar{1}$0) direction, which suggests the quasi-3D nature of the electron gas state with valley degeneracy $v_v = 12$, distinctly different from the pure 2D nature

of electron gas in widely reported oxide heterostructures, e.g., LAO/STO. Elastic neutron scattering measurements verify the ferrimagnetic ordering in the SCMO thin films, which, together with the interfacial Ti^{3+} spins due to oxygen deficient, possibly contributes to spin polarization of the electron gas and thus results in the negative MR effect at low temperatures. This electron gas system with high valley degeneracy and quasi-3D characteristics provides perspective to the well-studied 2DEG in oxide heterostructures wherein the valley degeneracy at the interface were largely ignored, and offers a potential materials category (double perovskites) to construct heterointerfaces with valley degeneracy electron gas.

Methods

Preparation of Sr_2CrMoO_6 ceramic target

A ceramic target with nominal composition of Sr_2CrMoO_6 was prepared by the conventional solid-state reaction method using stoichiometric Sr ($SrCO_3$ (99.95%)), Cr (Cr_2O_3(99.95%)), and Mo (MoO_3 (99.95%)) as starting materials. The starting materials were well mixed via ball milling for 20 h and sintered at 950 °C for 12 h to complete the chemical reaction. The obtained polycrystal sample was further grounded into a fine powder via 20 h ball milling, and cold-pressed into a pellet. The pellet was sintered at 1100 °C for 12 h to obtain the ceramic target with a diameter of 25 mm.

Thin film growth

A pulsed laser deposition apparatus equipped with a KrF ($\lambda = 248$ nm) excimer laser was employed to grow Sr_2CrMoO_6 (SCMO) thin films on one-side polished (110)-oriented $SrTiO_3$ (STO) single-crystal substrates. Since the target and thin film are in different chemical compositions, high-vacuum conditions are necessary to guarantee low-oxygen thin film deposition. Before deposition, the chamber was pumped into high vacuum with a pressure of 5.0×10^{-5} Pa. The deposition process was carried out at 5.0×10^{-4} Pa for 30 min with a substrate temperature of 775 °C, followed by in-situ annealing for 30 min. Then the film was in-situ (5.0×10^{-4} Pa) cooled down to room temperature at a rate of 10 °C/min. The distance between the target and the substrate was set at 5 cm. The laser energy density and repetition rate are 1 J/cm^2 and 2 Hz, respectively. The film thickness is controlled by the number of laser pulses.

Structural characterization

The structural properties of the SCMO film were characterized via X-ray diffraction (XRD) rocking curve, θ–2θ and φ scans, and reciprocal space mapping using an X-ray diffractometer (SmartLab Rikagu) equipped with Cu $K\alpha_1$ radiation ($\lambda = 1.5406$ Å). Atomic force microscopy (AFM) images were measured at room temperature using an Oxford Cypher ES device. High-angle annular dark-field scanning transmission electron microscopy (HAADF-STEM) images were measured using a FEI titan themis 200 transmission electron microscope. The specimen for HAADF-STEM measurements was prepared using a FEI Helios 450 S dual beam focused ion beam (FIB).

Electronic transport measurements

A layer of silver (Ag) film was deposited onto the surface electrode region of the SCMO film to form ohmic contacts and increase the stickness for wire bonding. Then, aluminum (Al) wires were directly bonded to the SCMO/STO interface using the conventional ultrasonic wire bonding approach. Magnetotransport measurements up to 14 T were performed using a Physical Property Measurement System (PPMS) (DynaCool-14, Quantum Design). The rotation angle magnetoresistance measurements were conducted via a vertical rotator mounted on the PPMS. The magnetoresistance at temperatures below 1.8 K was measured using a diluted refrigerator equipped with an Oxford magnet (Triton 500, Oxford Instruments).

Elastic neutron scattering measurements

To enhance the neutron scattering signal, a SCMO thin film with a thickness of ~1 μm was deposited on a 10×10 mm^2 substrate (total mass ~0.6 mg). The elastic neutron scattering measurement was conducted using the Taipan triple-axis spectrometer based at the OPAL research reactor in Lucas Heights, Australia. By selecting the exact wavelength of both the incident and scattered neutrons at Taipan, purely elastic scattering could be measured without the usual background contribution from inelastic scattering that is typically observed in diffraction experiments. During elastic scattering, the neutron wavelength of $\lambda = 2.34$ Å was employed. Pyrolytic graphite filters was placed both before and after the sample to suppress higher-order wavelengths. During measurements, the thin-film sample was mounted in a top-loading cryostat, with a 3–800 K temperature range.

Data availability

All data needed to evaluate the conclusions of the paper are present in the paper and/or Supplementary Information. Additional data related to this paper may be requested from the authors.

Received: 12 November 2023; Accepted: 11 March 2024;
Published online: 22 March 2024

References

1. Ohtomo, A. & Hwang, H. A high-mobility electron gas at the $LaAlO_3$/$SrTiO_3$ heterointerface. *Nature* **427**, 423–426 (2004).
2. Noel, P. et al. Non-volatile electric control of spin-charge conversion in a $SrTiO_3$ Rashba system. *Nature* **580**, 483–486 (2020).
3. Santander-Syro, A. F. et al. Two-dimensional electron gas with universal subbands at the surface of $SrTiO_3$. *Nature* **469**, 189–193 (2011).
4. Ohta, H. et al. Giant thermoelectric seebeck coefficient of two-dimensional electron gas in $SrTiO_3$. *Nat. Mater.* **6**, 129–134 (2007).
5. Smink, A. E. M. et al. Gate-tunable band structure of the $LaAlO_3$/$SrTiO_3$ interface. *Phys. Rev. Lett.* **118**, 106401 (2017).
6. Sun, Y. Q. et al. Critical thickness in superconducting $LaAlO_3$/$KTaO_3$ (111) heterostructures. *Phys. Rev. Lett.* **127**, 086804 (2021).
7. Verissimo-Alves, M., Garcia-Fernandez, P., Bilc, D. I., Ghosez, P. & Junquera, J. Highly confined spin-polarized two-dimensional electron gas in $SrTiO_3$/$SrRuO_3$ superlattices. *Phys. Rev. Lett.* **108**, 107003 (2012).
8. Zhang, H. et al. High-mobility spin-polarized two-dimensional electron gases at EuO/$KTaO_3$ Interfaces. *Phys. Rev. Lett.* **121**, 116803 (2018).
9. Liu, C. J. et al. Two-dimensional superconductivity and anisotropic transport at $KTaO_3$ (111) interfaces. *Science* **371**, 716–721 (2021).
10. Camjayi, A., Haule, K., Dobrosavljević, V. & Kotliar, G. Coulomb correlations and the Wigner–Mott transition. *Nat. Phys.* **4**, 932–935 (2008).
11. Caviglia, A. et al. Tunable Rashba spin-orbit interaction at oxide interfaces. *Phys. Rev. Lett.* **104**, 126803 (2010).
12. Shalom, M. B., Sachs, M., Rakhmilevitch, D., Palevski, A. & Dagan, Y. Tuning spin-orbit coupling and superconductivity at the $SrTiO_3$/$LaAlO_3$ interface: a magnetotransport study. *Phys. Rev. Lett.* **104**, 126802 (2010).
13. Sanyal, P. et al. Magnetism in Sr_2CrMoO_6: a combined ab initio and model study. *Phys. Rev. B* **94**, 035132 (2016).
14. Wang, Z.-C. et al. Giant linear magnetoresistance in half-metallic Sr_2CrMoO_6 thin films. *npj Quantum Mater.* **6**, 53 (2021).
15. Arulraj, A., Ramesha, K., Gopalakrishnan, J. & Rao, C. Magnetoresistance in the double perovskite Sr_2CrMoO_6. *J. Solid. State Chem.* **155**, 233–237 (2000).
16. Patterson, F. K., Moeller, C. W. & Ward, R. Magnetic oxides of molybdenum (V) and tungsten (V) with the ordered perovskite structure. *Inorg. Chem.* **2**, 196–198 (1963).
17. Kobayashi, K.-I., Kimura, T., Sawada, H., Terakura, K. & Tokura, Y. Room-temperature magnetoresistance in an oxide material with an ordered double-perovskite structure. *Nature* **395**, 677–680 (1998).
18. Philipp, J. et al. Spin-dependent transport in the double-perovskite Sr_2CrWO_6. *Appl. Phys. Lett.* **79**, 3654–3656 (2001).

19. Chan, T. S. et al. Structural, electrical and magnetic characterization of the double perovskites Sr_2CrMO_6 (M= Mo, W): B′ 4d–5d system. *Solid State Commun.* **131**, 531–535 (2004).
20. Zhang, J. et al. Giant positive magnetoresistance in half-metallic double-perovskite Sr_2CrWO_6 thin films. *Sci. Adv.* **3**, e1701473 (2017).
21. Caviglia, A. D. et al. Two-dimensional quantum oscillations of the conductance at $LaAlO_3/SrTiO_3$ interfaces. *Phys. Rev. Lett.* **105**, 236802 (2010).
22. Chen, Y. Z. et al. A high-mobility two-dimensional electron gas at the spinel/perovskite interface of γ-$Al_2O_3/SrTiO_3$. *Nat. Commun.* **4**, 1371 (2013).
23. Sánchez, D. et al. Origin of neutron magnetic scattering in antisite-disordered Sr_2FeMoO6 double perovskites. *Phys. Rev. B* **65**, 104426 (2002).
24. Danilkin, S. A., Horton, G., Moore, R., Braoudakis, G. & Hagen, M. The TAIPAN thermal triple-axis spectrometer at the OPAL. *React. J. Neut. Res.* **15**, 55 (2007).
25. Stornaiuolo, D. et al. Tunable spin polarization and superconductivity in engineered oxide interfaces. *Nat. Mater.* **15**, 278–283 (2016).
26. Harrang, J. P. et al. Quantum and classical mobility determination of the dominant scattering mechanism in the two-dimensional electron gas of an AlGaAs/GaAs heterojunction. *Phys. Rev. B* **32**, 8126 (1985).
27. Van Delft, M. R. et al. Electron-hole tunneling revealed by quantum oscillations in the nodal-line semimetal HfSiS. *Phys. Rev. Lett.* **121**, 256602 (2018).
28. Allen, S. J. et al. Conduction-band edge and Shubnikov–de Haas effect in low-electron-density $SrTiO_3$. *Phys. Rev. B* **88**, 045114 (2013).
29. Uwe, H., Yoshizaki, R., Sakudo, T., Izumi, A. & Uzumaki, T. Conduction band structure of $SrTiO_3$. *Jpn. J. Appl. Phys.* **24**, 335 (1985).

Acknowledgements

This work was supported by the National Natural Science Foundation of China (Grant No. 11974155), Natural Science Foundation of Guangdong Province (Grant No. 2022A1515010583), and Bureau of Education of Guangzhou Municipality (Grant No. 202255464). We acknowledge the support from ANSTO for Taipan proposal P9901 and the support from ARC Centre of Excellence in Future Low-Energy Electronics Technologies (Grant No. CE170100039). J.K. and W.Z. acknowledge Australian Research Council Discovery Project (Grant No. DP200102477). W.Z. acknowledges the support of PGRA and ECRG from AINSE. J.Y.D. acknowledges the financial support from Hong Kong GRF grant (No: 15301421). M.Y. and L.C. acknowledge the financial support from the National Natural Science Foundation of China (Grant No. 51972160).

Author contributions

R.K.Z. and W.Z. supervised the research. Z.C.W. and S.S.L. prepared thin films and performed transport measurements. Y.Z., S.J.Z., J.S.Y., and F.S.L. performed XRD, AFM, and STEM measurements. T.W.C. performed mK-SdH measurements. M.Y. and Lang Chen performed magnetic measurements. D.C., W.Z., and K.R. performed elastic neuron scattering measurements and analyzed the data. J.K., J.Y.D., D.F.L., and X.L.W. contributed to the discussion and revision of the manuscript. Z.C.W., Lei Chen, W.Z. and R.K.Z. wrote the manuscript with input from all authors. All authors discussed the results and commented on the manuscript.

Competing interests

The authors declare no competing interests.

Additional information

Supplementary information The online version contains supplementary material available at https://doi.org/10.1038/s42005-024-01597-7.

Correspondence and requests for materials should be addressed to Weiyao Zhao or Ren-Kui Zheng.

Peer review information *Communications Physics* thanks the anonymous reviewers for their contribution to the peer review of this work.

Reprints and permissions information is available at http://www.nature.com/reprints

Publisher's note Springer Nature remains neutral with regard to jurisdictional claims in published maps and institutional affiliations.

[1]School of Physics and Materials Science and Jiangxi Engineering Laboratory for Advanced Functional Thin Films, Nanchang University, Nanchang 330031, China. [2]School of Physics and Materials Science, Guangzhou University, Guangzhou 510006, China. [3]Department of Materials Science & Engineering, Monash University, Clayton, VIC 3800, Australia. [4]ARC Centre of Excellence in Future Low-Energy Electronics Technologies, Monash University, Clayton, VIC 3800, Australia. [5]School of Materials and Mechanic & Electrical Engineering, Jiangxi Science and Technology Normal University, Nanchang 330038, China. [6]School of Physics and Electronic Information, Gannan Normal University, Ganzhou 341000, China. [7]Department of Physics, Southern University of Science and Technology, Shenzhen 518055, China. [8]Department of Physics, City University of Hong Kong, Hong Kong, China. [9]Australia's Nuclear Science and Technology Organization, New Illawarra Rd, Lucas Heights, NSW 2234, Australia. [10]Institute for Superconducting and Electronic Materials and ARC Centre of Excellence for Future Low-Energy Electronics Technologies (FLEET), Australian Institute for Innovative Materials, University of Wollongong, North Wollongong, NSW 2500, Australia. [11]Department of Applied Physics, The Hong Kong Polytechnic University, Hong Kong, China. [12]Research Center for Advanced Information Materials (CAIM), Huangpu Research and Graduate School of Guangzhou University, Guangzhou 510006, China. [13]Key Lab of Si-based Information Materials & Devices and Integrated Circuits Design, Department of Education of Guangdong Province, Guangzhou 510006, China. [14]These authors contributed equally: Zhao-Cai Wang, Lei Chen. ✉e-mail: weiyao.zhao@monash.edu; zrk@ustc.edu